Dynamic update of flow and transport parameters in reactive transport simulations of radioactive waste repositories

Jesús F. Águila[1], Javier Samper[1]*, Alba Mon[1] & Luis Montenegro[1]

1. Centro de Investigaciones Científicas Avanzadas (CICA). Escuela Técnica Superior de Ingenieros de Caminos, Canales y Puertos. Universidad de A Coruña. Campus de Elviña, University of A Coruña, 15071 A Coruña, Spain

*Corresponding author. E-mail address: j.samper@udc.es

ABSTRACT

The changes in porosity caused by mineral dissolution/precipitation and the associated changes in flow, transport and chemical parameters of porous and fractured media are relevant for the geochemical time-evolution of natural and engineered underground systems. The realistic representation of natural systems requires modeling tools accounting for the changes in porosity. Here, we investigate the significance of the dynamic upgrade of the flow, transport and chemical parameters in reactive transport models with mineral dissolution/precipitation. The water flow, heat transfer and multicomponent reactive solute transport code, CORE^{2D}V5, was extended to take into account the changes in porosity provoked by mineral dissolution/precipitation and their effect on flow, solute transport and chemical parameters. The improvements implemented in the code were verified against analytical solutions and the numerical solutions computed with other reactive transport codes with similar capabilities for isothermal mineral dissolution/precipitation test cases. Model results computed with CORE^{2D}V5 agree with the analytical and numerical solutions for several isothermal test cases with porosity feedback. Model results show that failing to account for the porosity feedback leads to large errors. The porosity feedback effect (PFE) is

especially relevant in long-term problems with mineral dissolution/precipitation leading to strong changes in porosity. The PFE is analyzed with a non-isothermal geochemically-reactive transport model of the long-term ($4 \cdot 10^4$ years) interactions of compacted bentonite with corrosion products and concrete in a high-level radioactive waste repository in clay. The model predicts pore clogging in the concrete and at the concrete-clay interface. The thickness of the zone affected by pore clogging computed with the PFE is smaller than that computed without the PFE.

Keywords: Reactive transport model; CORE^{2D}V5; Porosity feedback effect; Pore clogging, radioactive waste disposal, non-isothermal

1. Introduction

Groundwater flow, heat transfer, and reactive solute transport models are useful tools for understanding natural groundwater bodies, quantifying groundwater pollution and evaluating the performance of waste disposal facilities (Steefel et al., 2005). Reactive transport models have been used within the following realms: 1) Geothermal systems (Alt-Epping et al., 2013a, 2013b; Wanner et al., 2014, 2017; Diamond and Alt-Epping, 2014; Xu et al., 2016), 2) Geological radioactive waste disposal (Yllera et al., 2004; De Windt et al., 2004; Molinero et al., 2004; De Windt et al., 2007; Samper et al., 2008, 2016; Soler et al., 2008; Zhang et al., 2008; Lu et al., 2011; Zheng et al., 2010, 2011, 2017; Berner et al., 2013; Kosakowski and Berner, 2013; Mon et al., 2017; Samper et al., 2018), 3) Geological carbon dioxide storage (Bildstein et al., 2010; Yang et al., 2011, 2014; Wei et al., 2015; Dai et al, 2016, 2018; Todaka and Xu, 2017) and 4) Environmental remediation (Samper and Yang, 2006; Yang et al., 2008; Jamieson-Hanes et al., 2012; Wanner et al., 2012; Wanner and Sonnenthal, 2013; Yeh et al., 2013).

Modern reactive transport codes are able to consider a wide range of equilibrium and kinetically controlled biogeochemical reactions, such as: 1) Homogeneous reactions (aqueous complexation, acid-base and redox reactions), 2) Mineral dissolution and precipitation reactions, 3) Multisite surface complexation, 4) Multisite ion exchange reactions, 5) Gas–aqueous phase exchange, and

6) Microbial reactions. Steefel et al. (2015) described the mathematical and numerical formulations used in numerical reactive transport codes that consider continuum representations of flow, transport and reactions in porous media. This approach uses a macroscopic scale by averaging system properties. Experimental data are essential to reduce the uncertainties in the parameters and geochemical processes of continuum-scale reactive transport models (Katz et al., 2011; Fox et al., 2015; Poonoosamy et al., 2015, 2016, Shafizadeh et al., 2020). The solution of the inverse problem of multicomponent reactive solute transport provides a way to determine unknown flow and transport parameters by using experimental data (Samper et al., 2006; Dai et al., 2009, 2012; Wolfsberg et al., 2018). However, the continuum approach is not valid to study geochemical reactions and the processes controlling the evolution of porous media that occur at the pore scale. In recent years, significant progress has been made in pore scale investigations (Molins 2015; Seigneur et al., 2017; Deng et al., 2018). Nevertheless, it is not yet feasible to simulate reactive transport on larger scales (m - km) by using pore scale approaches.

Numerical simulations of systems in which the dissolution/precipitation of minerals may lead to significant changes in the porosity are complex because the changes in porosity can modify the fluid flow and influence transport and chemical reaction parameters (Chagneau et al, 2015; Min et al., 2016). The porosity feedback effect under isothermal conditions is accounted for in computer codes such as HYTEC (van der Lee et al., 2003), TOUGHREACT (Xu et al., 2004, 2006, 2011), HYDRUS1D-PHREEQC (Simunek et al. 2008, 2009), MIN3P (Mayer et al., 2002), PHAST (Parkhurst et al., 2002), CRUNCH (Steefel, 2001) and PFlotran (Hammond et al., 2014; Lichtner et al., 2018). The implementations of the porosity feedback in the reactive transport codes is commonly verified by comparing numerical results with analytical solutions. However, only a few analytical solutions for the porosity feedback effect (PFE) are available in the literature (Lagneau and van der Lee, 2010; Hayek et al., 2011; 2012). Code verification is possible by comparing model results computed with several codes for appropriate benchmark cases (Xie et al., 2015; Poonoosamy et al., 2018). Chen and Liu (2002) developed a method to solve a set of

nonlinear equations coupled with fluid flow, species transport and rock/fluid reactions including the alteration of porosity and permeability due to mineral-fluid reactions. Shao et al. (2013) used a numerical model to study the geochemical iterations and the induced changes in the porosity (clogging) in the Maqarin marl rock (Jordan). Seigneur et al. (2018) developed an algorithm to couple accurately the feedback of chemistry on water consumption, variable porosity and flow in variably-saturated reactive transport models. Seigneur et al. (2019) reviewed equations of multiphase flow and reactive transport on the continuum scale, the recent studies carried out on the pore scale and provided a summary of the more common approaches used to describe evolving flow and transport parameters due to mineral dissolution/precipitation reactions in reactive transport models.

The CORE series of reactive transport codes have been developed at the University of A Coruña since 1991. CORE^{2D}V4 (Samper et al., 2009; 2011) is one of these codes for transient saturated and unsaturated water flow, heat transport and multicomponent reactive solute transport under both local chemical equilibrium and kinetic conditions. The flow and transport equations are solved with Galerkin finite elements and an Euler scheme for time discretization. The chemical formulation is based on the ion association theory while the extended version of Debye-Hückel equation (B-dot) is used to calculate the activity coefficients of aqueous species. CORE^{2D}V4 uses the EQ3/6 "*com"* thermodynamic database (Wolery, 1992). The codes of the CORE series have been widely used to simulate geological radioactive waste disposal facilities that envisage several engineered barriers such as a metallic canister and a compacted bentonite barrier. Mon et al. (2017) presented a non-isothermal reactive transport model to simulate the long-term evolution of a geological repository in clay and quantify the interactions at the interfaces of compacted bentonite, canister and concrete. This model was calculated with CORE^{2D}V4 by assuming a constant porosity. Failing to account for the changes in porosity, ϕ, may lead to unrealistic results with porosities out of the feasible interval ($0 < \phi < 1$).

99 Here we investigate the significance of the dynamic update of the flow, transport and chemical
100 parameters in reactive transport models with mineral dissolution/precipitation. CORE^{2D}V5 has
101 been developed from CORE^{2D}V4 to take into account the PFE due to mineral
102 dissolution/precipitation under isothermal and non-isothermal conditions. CORE^{2D}V5 has been
103 verified with one- and two-dimensional analytical solutions (Hayek et al., 2011; 2012). In
104 addition, numerical solutions obtained with the two versions of the code CORE^{2D} with and
105 without the PFE have been compared with analytical solutions to illustrate the significance of the
106 PFE in reactive transport models with mineral dissolution/precipitation. The benchmark proposed
107 by Xie et al. (2015) has also been used to verify the code against other reactive transport codes.
108 Furthermore, the capabilities of CORE^{2D}V5 have been used to evaluate the importance of the PFE
109 on the long-term geochemical evolution of a radioactive waste repository in clay by using the
110 reactive transport model of Mon et al. (2017), which has been extended to account for the PFE.
111 To the best of our knowledge, this is the first time that the importance of the PFE is studied for
112 radioactive waste disposal under non-isothermal conditions. The paper presents first the
113 mathematical formulation of the non-isothermal reactive transport and the dynamic update of the
114 permeability, the diffusion coefficient and the specific mineral surface. Then, the numerical
115 implementation in CORE^{2D}V5 is described. Several verification and benchmarking cases are
116 presented later. Afterwards, the reactive transport model of the long-term geochemical evolution
117 of a radioactive waste repository in clay is presented.

118 2. Mathematical formulation

119 CORE^{2D}V5 is a numerical code that solves simultaneously the equations governing groundwater
120 flow, heat transport and geochemically-reactive solute transport. The water flow in variably
121 saturated porous media is given by (Xu et al., 1999):

122 $$\nabla \cdot [K_r \boldsymbol{K} \nabla(\Psi + z)] + w = \left(\phi \frac{\partial S_w}{\partial \Psi} + S_w S_s\right) \frac{\partial \Psi}{\partial t} \quad (1)$$

123 The definition of all the symbols used can be found in the Nomenclature. When the diffusion and
124 dispersion coefficients are similar for all the aqueous species, the reactive transport equations can
125 be expressed in terms of total dissolved component concentrations, C_k, (Xu et al., 1999):

126 $$\nabla \cdot (\theta \boldsymbol{D} \nabla C_k) - \boldsymbol{q} \nabla (C_k) + w(C_k^* - C_k) + \theta R_k = \frac{\partial (\theta C_k)}{\partial t} \qquad k = 1,2, \dots, N_c \tag{2}$$

127 The set of geochemical reactions consists of: homogeneous reactions such as aqueous
128 complexation, acid-base and redox reactions and heterogeneous reactions such as mineral
129 precipitation/dissolution, cation exchange, surface complexation and gas dissolution/exsolution
130 reactions. The aqueous chemical system is described in terms of N_c primary species. The rest of
131 the species, known as secondary species, can be represented as linear combinations of the primary
132 species. The total dissolved concentration of a primary species is given by (Xu et al., 1999):

133 $$C_k = c_k + \sum_{j=1}^{Nx} v_{jk} x_j = c_k + \sum_{j=1}^{Nx} v_{jk} \left(K_j^{-1} \gamma_j^{-1} \prod_{i=1}^{Nc} c_i^{v_{ji}} \gamma_i^{v_{ji}} \right) \tag{3}$$

134 Heat is transported in the water-solid matrix system by groundwater flow and thermal conduction
135 through the fluid and the solid. The heat transport equation is given by (Samper et al., 2011):

136 $$\nabla(\boldsymbol{\lambda} \nabla \mathrm{T} - \rho c_w \boldsymbol{q} T) = \theta \rho c_w \frac{\partial T}{\partial t} + (1 - \theta) \rho_s c_s \frac{\partial T_s}{\partial t} = \rho_m c_m \frac{\partial T}{\partial t} \tag{4}$$

137 CORE^{2D}V5 considers the changes in porosity and updates flow, transport and chemical
138 parameters. The porosity, ϕ, is updated each time step from the computed values of the mineral
139 volume fractions, f_m, according to:

140 $$\phi = 1 - \sum_{m=1}^{N_p} f_m \tag{5}$$

141 The changes in the permeability are calculated from the Kozeny-Carman equation (Carman,
142 1937). This is one of the most widely accepted permeability-porosity relationships which relates
143 the properties of the porous medium to the flow resistance in pore channels. The Kozeny-Carman
144 equation provides an expression to relate the permeability, k, to the porosity through:

$$k = k_0 \frac{(1-\phi_0)^2}{(1-\phi)^2}\left(\frac{\phi}{\phi_0}\right)^3 \quad (6)$$

The pore diffusion coefficients are updated by using the Archie's law (Archie, 1942) which describes the ratio between the effective diffusion of a solute in a porous medium and its diffusion coefficient in pure water which depends on the tortuosity of the medium and the constrictivity. This ratio is often described in terms of the geometrical factor:

$$\frac{D_e}{D_0} = \frac{\delta}{\tau} = \phi^m \quad (7)$$

CORE^{2D}V5 uses the following kinetic rate law for mineral dissolution/precipitation reactions:

$$r_m = s_m k_m e^{\frac{-Ea}{RT}}\left(\prod_{i=1}^{N_C+N_X} a_i^{p_{mi}}\right)\left(\Omega_m^{\Theta_m} - 1\right)^{\eta_m} \quad (8)$$

The specific surface of the minerals in saturated porous media (expressed as the surface of mineral per unit volume of water) is updated each time step according to:

$$A_m^{t+1} = A_m^t \frac{\phi^t}{\phi^{t+1}} \quad (9)$$

Eqs (6), (7), (9) are commonly used in reactive transport models based on the continuum approach to update flow and transport parameters from the changes in porosity provoked by mineral dissolution/precipitation (Steefel et al., 2015; Hommel et al. 2018; Poonoosamy et al., 2018). Although these empirical relationships may not be physically representative of the pore-scale processes (Seigneur et al., 2019), they have proven useful to provide a quantitative interpretation of observational data under dynamic conditions.

3. Numerical implementation in CORE^{2D}V5

CORE^{2D}V5 uses a Sequential Iteration Approach (SIA) to solve the coupled solute transport equations and hydrogeochemical reactions. In this approach, transport and chemical equations are treated as two different systems which are solved separately in a sequential iterative process (Xu

et al., 1999; Samper et al., 2011). The set of chemical equations is solved on a node basis after solving the transport equations. The resulting non-linear equations are solved with an iterative Newton-Raphson method.

CORE^{2D}V5 has been extended to consider the PFE. It should be noticed that the computational work increases when the PFE is considered. Alternatively, CORE^{2D}V5 can also compute the changes in porosity from changes in mineral volume fractions without considering the PFE. If the porosity feedback is modeled, the code checks that the sum of the porosity and the mineral volume fractions is equal to 1 in all the nodes of the grid. In addition, a minimum threshold porosity for clogging is defined by the user.

The porosity is updated each time step according to Eq. (5). Minerals are not allowed to precipitate anymore when the porosity is smaller than the threshold porosity. However, mineral dissolution is still allowed although porosity reaches the threshold value. Permeability is updated in the flow equation each time step based on the Kozeny-Carman equation (see Eq. (6)). Nodal water volumes are updated with the most recent values of the porosities after solving the flow equations. Groundwater velocities which are required to evaluate advective and dispersive solute and heat fluxes are calculated from nodal heads by direct application of Darcy's Law to the finite element solution. Diffusion coefficients are updated according to Archie's law (see Eq. (7)). The concentrations of dissolved species are calculated in mol per unit volume of water. Nodal water volumes and the concentrations of dissolved are updated each time step to account for the changes in the porosity. Mineral specific surfaces in saturated porous media are updated each time step according to Eq. (9). Model results related to the changes in porosity are printed out over time in selected output files created by CORE^{2D}V5.

Fig. 1 shows the main flowchart of CORE^{2D}V5 with an indication of the main modifications performed in the code to consider the PFE.

4. Verification

4.1. Verification with analytical solutions

The improvements implemented in CORE^{2D}V5 have been verified with the analytical solutions presented by Hayek et al. (2011, 2012). They provided a general methodology to derive analytical solutions for diffusive transport of aqueous species coupled to dissolution/precipitation of a single mineral with a strong PFE. They also reported several examples for 1-D and 2-D systems to use analytical solutions for code benchmarking. CORE^{2D}V5 was verified with the analytical solutions for a mineral $M_{(s)}$ initially at chemical equilibrium with two aqueous species $A_{(aq)}$ and $B_{(aq)}$. Then, $M_{(s)}$ dissolves with a kinetic control according to the following chemical reaction:

$$A_{(aq)} + B_{(aq)} \leftrightarrow M_{(s)} \tag{10}$$

The analytical solutions assume that solute diffusion is the only transport mechanism. The effective diffusion coefficient is assumed to be proportional to porosity ($D_e = D_0\,\phi$). The following kinetic mineral dissolution/precipitation rate law is used:

$$R_m = r_m A_m \left[1 - \frac{c_1 c_2}{K}\right] \tag{11}$$

where c_1 and c_2 are the concentrations of species A and B, respectively, and A_m is the solid reactive surface area which is equal to $A_0\,\phi$, where A_0 is a constant.

4.1.1. 1-D verification test case

The results computed with the 1-D numerical model performed with CORE^{2D}V5 were compared with the analytical solutions of Hayek et al. (2011) (see Eq. (A.1), Eq. (A.2) and Eq. (A.3) in the Supplementary Material). The model domain has a length equal to 0.05 m and it was discretized with a regular 1-D finite element grid with 50 elements and 51 nodes. The concentration of the species B is uniform in space and constant in time (c_2 = 1 mol/ kg H_2O). Initially, each node of the grid has a different value of c_1 and ϕ. In addition, c_1 is fixed at the boundaries of the model (x

213 = 0 and x = 0.05 m) with time functions obtained from Eq. (A.1). The simulation was run for 10^5
214 s with time increments of 1 s. 1-D model parameters are listed in Table 1.

215 The computed concentration profiles of species A at several times agree with those calculated
216 with the analytical solutions (see Fig. 1S in the Supplementary Material). c_1 at the left boundary
217 increases with time while it remains unchanged at the right boundary. Fig. 2 shows the comparison
218 of the computed and analytical porosity profiles. Numerical and analytical solutions agree very
219 well. The porosity at the left boundary of the model decreases considerably with time, reaching
220 very small values (clogging).

221 The computed mineral concentration (in mol/m^3 of fluid and in mol/m^3 of rock) were also
222 compared with analytical solutions (see Fig. 3 and Fig. 2S). The results computed with
223 CORE^{2D}V5 agree with the analytical solutions. The mineral concentration in mol per m^3 of fluid
224 volume near the left boundary reaches very high values while the mineral concentration in mol
225 per m^3 of rock volume reaches a constant value when the porosity tends to zero.

226 The significance of the PFE is illustrated by comparing the porosity and the mineral concentration
227 profiles computed with and without the PFE (Fig. 2 and 3). The porosity decreases more quickly
228 in the run without the PFE. The extent of the model in which the clogging occurs in the run
229 without the PFE is larger than in the run with the PEF. The PFE is particularly relevant in models
230 with mineral dissolution/precipitation reactions leading to strong changes in porosity.

231 **4.1.2. 2-D verification test case**

232 The improvements implemented in CORE^{2D}V5 for two-dimensional problems have been verified
233 with an exact analytical solution proposed by Hayek et al. (2012). The 1 m x 1 m model domain
234 was discretized with a triangular mesh with 736 elements and 406 nodes (Fig. 3S). The simulation
235 was performed for $1.5 \cdot 10^7$ s. The time domain was divided into 1500 time periods which in turn
236 were subdivided into 100 time increments.

406 different mineral zones and initial waters were defined in the numerical model (one per node) to define the initial porosities and the nodal concentrations of species A and B obtained from Eq. (A.4), Eq. (A.5) and Eq. (A.6) (see Appendix A in the Supplementary Material). The time functions calculated with Eq. (A.4) and Eq. (A.5) were used to prescribe the concentrations c_1 and c_2 at the nodes located along the boundaries of the model, respectively. 2-D model parameters are listed in Table 1.

Fig. 4S and Fig. 5S show the comparison of the analytical and numerical concentration profiles of species A and B along the first 40 cm of the diagonal of the model domain for selected times. c_1 and c_2 at the lower left corner increase with time while they remain constant in the middle of the domain ($c_2 \approx 2c_1$). The numerical solutions coincide with the analytical solutions. The product of c_1c_2 increases exponentially at the lower left corner of the model domain. Consequently, the mineral $M_{(s)}$ precipitates strongly at the lower left corner because $c_1c_2 > K$ (see Eq. 11). Fig. 4 shows 3-D plots of the spatial distribution of the porosity computed with the analytical and numerical solutions at $5 \cdot 10^6$ s and $1.5 \cdot 10^7$ s. The porosity at the lower left corner of the model domain at the end of the simulation is very small (pore clogging).

A simulation run was performed with CORE^{2D}V5 without the PFE. The model results computed with and without the PFE at early times ($t = 5 \cdot 10^6$ s) are similar. Later, the differences in model results increase. The porosity decreases more quickly in the run without the PFE (Fig. 4). Fig. 5 shows the comparison of the porosity profiles computed with and without the PFE and the analytical solutions along the first 40 cm of the main diagonal of the model. Porosities computed with the PFE fully agree with those of the analytical solutions. However, the analytical and numerical solutions show significant differences when the PFE is not considered. The clogging effect is more important in the run without the PFE because the mineral precipitation is not restricted in this run.

4.2. Benchmarking

The previous analytical solutions correspond to initial and boundary conditions which are not typical of natural systems. CORE^{2D}V5 was verified also with a more realistic benchmark test case proposed by Xie et al. (2015). This benchmark considers 1D advective-dispersive transport, aqueous complexation and calcite and gypsum dissolution/precipitation. The Kozeny-Carman relationship and the Archie's law are used to relate the permeability, the tortuosity and the pore diffusion coefficient to the porosity, respectively. The simulation was performed at standard pressure (atmospheric pressure) and temperature (25º C) and water saturated conditions. The model domain is 2 m long. It was discretized with a uniform grid size of 0.125 m. The initial porosity and hydraulic conductivity are uniform and equal to 0.35 and $1.16 \cdot 10^{-4}$ m/s, respectively. The initial hydraulic head is equal to 0 in all the nodes of the grid. The hydraulic head is prescribed at the inflow (0.007 m) and outflow (0 m). The following kinetic rate law was used for mineral dissolution/precipitation reactions (Xie et al., 2015):

$$R_m = -r_m[1 - \Omega_m] \tag{12}$$

where r_m is rate constant for gypsum (a newly-formed mineral) which is updated as a function of the mineral volume fraction of calcite according to (Lichtner, 1996):

$$r_m^t = -r_m^0 \left(\frac{f_m^t}{f_m^0}\right)^{\frac{2}{3}} \tag{13}$$

Mineral parameters are listed in Table 2.

The simulation was performed for a time period of 1000 years. A sulfuric acid solution flows into the porous column containing initially calcite (f_m^0 = 0.30 m^3/m^3). The initial pore water is at chemical equilibrium with respect to calcite and undersaturated with respect to gypsum. The model accounts for five primary species and 13 aqueous complexes. The chemical composition

283 of the initial and boundary waters are listed in Table 3. Table 4 lists the equilibrium constants and
284 the aqueous complexation and mineral dissolution/precipitation reactions at 25 ºC.

285 CORE^{2D}V5 was verified with the model results computed with the code MIN3P (Xie et al., 2015).
286 Fig. 6 shows the comparison of the porosity profiles computed with MIN3P and CORE^{2D}V5 at
287 10, 100 and 1000 years. Initially, the porosity is uniform and equal to 0.35. Later, the porosity
288 changes due to the inflow of the acidic solution which leads to calcite dissolution and gypsum
289 precipitation (see Fig. 7 and Fig. 8). Model results show a calcite dissolution front near the inflow
290 boundary. Therefore, the porosity increases in the first 0.2 m of the model domain and reaches a
291 value equal to 0.65 after 10 years. The porosity at x = 0.2 m, however, declines due to gypsum
292 precipitation. The volume fraction of gypsum computed with CORE^{2D}V5 at x = 0.2 m is slightly
293 larger than that computed with MIN3P. Xie et al. (2015) reported some differences among codes
294 in this point. After 100 years, the length of the model where the porosity is equal to 0.65 increases
295 due to the advance of the calcite dissolution front. The precipitation of gypsum causes the
296 reduction of porosity and clogging occurs at x = 0.425 m. After 1000 years, the dissolution front
297 of calcite does not advance due to the clogging. The porosities and the volume fractions of calcite
298 and gypsum computed with CORE^{2D}V5 generally coincide with those calculated with MIN3P.

299 The hydraulic conductivities and the hydraulic heads computed with CORE^{2D}V5 are similar to
300 those computed with MIN3P (see Fig. 9 and Fig. 6S). Clogging occurs at t = 100 years and causes
301 a sharp decline of hydraulic heads and a drastic reduction in hydraulic conductivity at x = 0.425
302 m. The water outflow through the right boundary of the model is also affected by clogging (Fig.
303 7S). The calculated outflow decreases rapidly after 50 years of simulation. The time evolution of
304 the water outflow computed with CORE^{2D}V5 coincides with that of MIN3P.

305

306

5. Reactive transport modeling of a radioactive waste repository in clay

The model of Mon et al. (2017) has been extended by considering the PFE with CORE^{2D}V5. The results calculated with and without the PFE have been compared up to $t = 4 \cdot 10^4$ years. This time was selected because the thermal gradients dissipate fully after $2 \cdot 10^4$ years and the changes in porosity become especially relevant also after such period of time. The same spatial discretization has been used in both models to make more reliable the model intercomparison in the clogging zones (Marty et al., 2009). The model reported by Mon et al. (2017) corresponds to a radioactive waste repository in clay according to the Spanish Reference Concept. The waste is confined in cylindrical carbon steel canisters (0.9 m diameter) emplaced in horizontal galleries excavated in the clay formation. The galleries are protected with a 0.3 m thick concrete support. The canisters are surrounded by a 0.75 m thick bentonite barrier. The model assumes axial symmetry with respect to the gallery axis (Fig. 10). The numerical model takes into account the time evolution of the temperature in the repository (see Fig. 8S).

The reactive transport model considers the following chemical reactions: 1) Canister corrosion, 2) Aqueous reactions such as acid/base, redox and aqueous complexation reactions, 3) Surface complexation of Fe^{2+} and H^+ on three types of sorption sites; 4) Cation exchange of Ca^{2+}, Mg^{2+}, Na^+, K^+ and Fe^{2+} and 5) Dissolution/precipitation of 16 minerals. The aqueous chemical system includes 58 aqueous complexes and the following primary species: H_2O, Cl^-, SO_4^{2-}, HCO_3^-, $AlOH_4^-$, H^+, Ca^{2+}, Mg^{2+}, Na^+, K^+, Fe^{2+}, SiO_2(aq) and O_2(aq). All the reactions are assumed at local chemical equilibrium, except for smectite dissolution and canister corrosion. The corrosion rate is 2 μm/year. The thermal and hydrodynamic model parameters are listed in Table 5. More details about the model can be found in Mon et al. (2017).

The porosity in the model calculated with CORE^{2D}V5 is updated according to Eq. (5). The porosity is not allowed to be less than a threshold value. As an educated guess, this threshold is taken equal to 10^{-4}. The pore diffusion coefficients and the solute tortuosities are updated based

on Archie's law with a cementation exponent equal to 4/3 (Millington and Quirk, 1961; see Eq. (7)). Other flow, transport and chemical parameters such as nodal volumes, water velocities, mineral surface areas and nodal dissolved concentrations are also updated every time step to account for the changes in porosity. The dynamic update of the flow and transport parameters from changes in porosity is carried out in the bentonite, concrete and clay. The PFE is not taken into account in the nodes of the grid that simulate the canister.

Fig. 11 illustrates the radial distribution of the porosity at $t = 4 \cdot 10^4$ years computed with and without the PFE. Pore clogging in the concrete at $t = 4 \cdot 10^4$ years is predicted from $r = 1.33$ m to $r = 1.34$ m with the PFE and from $r = 1.24$ m to $r = 1.28$ m without the PFE. The pore clogging computed in the concrete near the clay interface is 2.5 cm without the PFE and clogging does not occur in the model with the PFE. The clogging thickness in the clay near the concrete interface is 0.8 cm and 1.7 cm with and without the PFE , respectively. Magnetite precipitation at the canister-bentonite interface ($r = 0.45$ m) causes pore clogging at $t = 4 \cdot 10^4$ years in the model without the PFE. However, porosity clogging does not occur in this area in the model with the PFE. The changes in porosity computed with the PFE greatly influence the radial distribution of the effective diffusion after $4 \cdot 10^4$ years (Fig. 9S).

The diffusion coefficient of the bentonite near the canister interface is reduced in the model with the PFE, causing that the precipitation of magnetite in the nodes of the canister near the canister-bentonite interface computed in the model with PFE is larger than in the model without PFE. For the same reason, model results with PFE show less magnetite precipitation in the bentonite near the canister interface than those without the PFE (see Fig. 13).

Fig. 12, Fig. 10S and Fig. 11S show the time evolution of the concentration of the cumulative mineral precipitation/dissolution in the bentonite (near the concrete interface at $r = 1.125$ m), the concrete (midpoint at $r = 1.35$ m) and the clay (near the interface at $r = 1.525$ m) computed with and without the PFE. Negative (positive) values correspond to mineral dissolution (precipitation).

Model results with the PFE show less brucite precipitation in the bentonite near the concrete interface (r = 1.125 m). Portlandite dissolution in the concrete midpoint computed with the model without the PFE is slightly faster than that computed with the PFE. All the portlandite is dissolved after $2 \cdot 10^4$ years in the model without the PFE and after $2.5 \cdot 10^4$ years in the model with the PFE. There are significant differences between the time evolution of the cumulative gypsum, brucite, sepiolite and calcite precipitation computed with and without PFE in the clay near the concrete interface (r = 1.525 m). Brucite starts precipitating during the first 10^4 years and later dissolves until $t = 3.5 \cdot 10^4$ years in the model with the PFE. Brucite precipitates slightly in the model with the PFE. Sepiolite precipitates in both simulations. However, the precipitation of sepiolite computed without the PFE is slightly larger than that of the model with the PFE. Gypsum precipitates at $t = 10^3$ years and dissolves later at $t = 10^4$ years in the simulation with the PFE. Calcite precipitates in both simulations. The precipitation of calcite in the model without the PFE is larger than in the model with the PFE during the first $2.4 \cdot 10^4$ years. Then, the precipitation of calcite in the model with the PFE is larger than in the model without the PFE.

Fig. 13 shows the mineral volume fractions at $t = 4 \cdot 10^4$ years computed with and without the PFE. The model with the PFE calculates less magnetite precipitation than the model without the PFE at the bentonite-canister interface. After $4 \cdot 10^4$ years, there is still portlandite in the concrete, from r = 1.23 m to r = 1.3 m, in the model without the PFE whereas portlandite remains from r = 1.24 m to r = 1.35 m in the model with the PFE. The results with the PFE show less precipitation of gypsum, brucite, sepiolite and analcime and more precipitation of calcite than those calculated without the PFE near the concrete-clay interface. The differences in the precipitation of brucite and sepiolite affect the pH after $4 \cdot 10^4$ years at both sides of the concrete-clay interface (see Fig. 14). Most of the published papers have addressed the PFE under isothermal conditions. The evaluation of the performance of geological radioactive waste disposal facilities requires the use of non-isothermal geochemically-reactive transport models because the radioactive waste generates heat and the thermal field and the temperature gradients may prevail for several

383 thousands of years. Fig. 14 illustrates clearly that the long-term evolution of the pH is clearly
384 affected by the temperature field for both constant and variable porosity models. These
385 predictions are consistent with the numerical findings of Samper et al. (2018) and experimental
386 observations of Lalan et al. (2016) which show that the temperature plays an important role in the
387 degradation of calcium silicate hydrate phases and the precipitation of mineral phases. The
388 changes in porosity for constant temperature are smaller than those computed under
389 nonisothermal conditions. Therefore, it can be concluded that there is a synergetic effect of
390 temperature and clogging.

391 The volume of the precipitated minerals may exceed the porosity of the medium in the most
392 reactive areas of the model domain. The model accounting for the PFE updates dynamically the
393 porosity and ensures that the total mineral volume fraction of the precipitated minerals does not
394 exceed the porosity. The model without the PFE, on the other hand, does not check whether the
395 total mineral volume fractions of the precipitated minerals exceed the porosity. The model results
396 computed with the model with the PFE are more realistic. A significant part of the differences
397 between the results computed with and without the PFE are related to the restriction in the porosity
398 imposed in the model which accounts for the PFE. The changes in the diffusion coefficient due
399 to changes in the porosity is another cause of the differences.

400 Although the mineral evolution computed with the model of the PFE show trends similar to those
401 of the model without the PFE, the results of both models show significant differences. Magnetite
402 precipitation in the model with the PFE is smaller than that computed with the model without the
403 PFE near the bentonite-canister interface due to the decrease of the diffusion coefficient in this
404 interface which favors more magnetite precipitation in the canister and no clogging at the
405 bentonite-canister interface. The pH in the concrete front computed with the model with the PFE
406 is sharper than that computed with the model without the PFE due to the drastic reduction in the
407 diffusion coefficient caused by the decrease in porosity. The total amounts of brucite, sepiolite

and gypsum precipitation at the concrete-clay interface computed with the model with the PFE is smaller than those computed with the model without the PFE due to the restriction on the porosity. For the most part, the concentrations of dissolved components computed with and without the PFE at $t = 4 \cdot 10^4$ years are similar. The radial distribution of solute concentrations show jumps at the location of pore clogging in the concrete ($r = 1.35$ m). These jumps are generally small except for dissolved SO_4^{2-} y $Al(OH)_4^-$ which show large jumps due to solute accumulation in the bentonite.

6. Conclusions

Most reactive transport models assume transport and chemical parameters such as porosity, permeability, pore diffusion coefficient and reactive surface areas of minerals remain constant in time. The significance of the dynamic upgrade of the flow, transport and chemical parameters in reactive transport models with mineral dissolution/precipitation has been investigated. The water flow, heat transport and geochemically-reactive solute transport code, CORE^{2D}V5, has been extended to take into account the PFE caused by mineral dissolution/precipitation reactions and update the flow, transport and chemical parameters. The porosity is updated each time step based on the changes in the volume fractions of the minerals computed in the previous time step. The permeability is updated by using a Kozeny-Carman equation while diffusion coefficients and tortuosities are updated according to Archie's law.

The improvements implemented in CORE^{2D}V5 have been verified with analytical solutions for diffusion problems coupled with dissolution/precipitation reactions and feedback of the changes in porosity in 1D and 2D. In addition, CORE^{2D}V5 has been verified against the numerical solutions of other reactive transport codes for a benchmark test case involving advective transport in a saturated medium with aqueous complexation and kinetic mineral dissolution/precipitation. The model results computed with CORE^{2D}V5 reproduce the analytical solutions and the numerical solutions computed with other reactive transport codes.

433 The numerical solutions computed with the updated version of CORE^{2D}V5 have been used to
434 illustrate the significance of the PFE for several tests cases. Although model results computed
435 with and without the PFE are similar at early times, they show large differences at late times. The
436 PFE is particularly relevant in problems with mineral dissolution/precipitation leading to strong
437 changes in porosity. The porosity decreases more quickly when the PFE is not taken into account.
438 The thickness of the clogging zones computed without the PFE is larger than that computed with
439 the PFE.

440 The updated version of CORE^{2D}V5 has been used to model the non-isothermal chemical
441 interactions of compacted bentonite, corrosion products and concrete in a radioactive waste
442 repository in clay by taking into account the PFE. The major differences of the porosity computed
443 with and without the PFE occur in the concrete and at the concrete-clay and canister-bentonite
444 interfaces. The thickness of pore clogging in the concrete and in the concrete-clay interface
445 computed with the PFE is smaller than that computed without the PFE. The zones affected by
446 clogging in the concrete at $t = 4 \cdot 10^4$ years computed with and without the PFE are 1 and 4 cm
447 thick, respectively. The thickness of clay affected by clogging near the concrete interface is 0.8
448 cm with the PFE while it is 1.7 cm without the PFE. In addition, there are zones affected by pore
449 clogging in the concrete near the clay interface and at the canister-bentonite interface in the model
450 without the PFE. However, porosity clogging does not occur in these areas in the model with the
451 PFE. On the other hand, there are significant differences in the mineral volume fractions
452 computed with and without the PFE after $4 \cdot 10^4$ years. The model with porosity the PFE calculates
453 less magnetite precipitation than the model without the PFE at the bentonite-canister interface.
454 The patterns of portlandite dissolution in the concrete computed with and without porosity the
455 PFE show differences. The model results computed with the PFE show less precipitation of
456 gypsum, brucite, sepiolite and analcime and more precipitation of calcite at the concrete-clay
457 interface than those calculated without the PFE. The largest differences in the computed pH after
458 $4 \cdot 10^4$ years occur at both sides of the concrete-clay interface.

459 The reactive transport models presented here demonstrated that the dynamic update of flow and
460 transport parameters is especially relevant in long-term problems with mineral
461 dissolution/precipitation reactions leading to strong changes in porosity. Modeling tools should
462 take into account the PFE when modeling both engineered systems and natural environments
463 where transport and chemical properties can vary significantly in space and time such as
464 radioactive waste disposal facilities, mine waste deposits and karst systems. However, numerical
465 simulations with the PFE have significant uncertainty. Realistic simulations of the changes in
466 porosity and clogging processes will require long-term experimental data to support model
467 results. Unfortunately, such experimental data are not widely available despite the significant
468 advances made recently in pore scale investigations. The conclusions of our numerical
469 simulations are relevant for the performance assessment of the engineered barriers of radioactive
470 waste repositories and will contribute to reduce model uncertainties and support the hypotheses
471 usually made in the evaluation of the long-term safety of the repositories.

472 The long-term geochemical predictions of the radioactive waste repository calculated with the
473 PFE presented here could be improved by: 1) Adopting a dynamic corrosion front to simulate
474 canister corrosion in a more realistic manner; 2) Simulating the dissolution/precipitation of all
475 minerals with kinetic laws and updating the reactive surface areas; and 3) Solving numerical
476 issues and reducing calculation times to take into account the PFE for a longer period of time (1
477 Ma).

478 ## Nomenclature

Latin terms	
A_m	specific surface of the *m*-th mineral
A_m^t, A_m^{t+1}	specific surface of the *m*-th mineral at times *t* and *t+1*
a_i^{pmi}	catalytic effect factor
C_k	total dissolved concentration of the *k*-th component
C_k^*	dissolved concentration of a fluid source *w*
c_i	molal concentrations of the *i*-th primary species
c_w c_s, c_m	specific heat of water, solids and bulk porous medium, respectively
$\boldsymbol{D}$	dispersion tensor
D_0	pore diffusion coefficient in pure water

D_e	effective diffusion coefficient
Ea	apparent activation energy
f_m	volume fraction of the m-th mineral
f_m^t, f_m^0	volume fractions of the m-th mineral at times t and $t = 0$, respectively
$\boldsymbol{K}$	saturated hydraulic conductivity tensor
K	mineral solubility constant
K_r	relative hydraulic conductivity
k, k_0	permeability and initial permeability, respectively
k_m	kinetic rate constant of the m-th mineral
$\boldsymbol{q}$	Darcy velocity
N_c	number of primary species
N_p	total number of minerals involved in dissolution/precipitation reactions
N_x	number of aqueous secondary species
m	cementation exponent
R	gas constant
R_k	chemical sink/source term of the k-th component
R_m	mineral dissolution/precipitation rate of the m-th mineral
r_m	effective dissolution/precipitation rate
r_m^t, r_m^0	effective dissolution/precipitation rates at times t and $t = 0$, respectively
s_m	factor for dissolution (1) and precipitation (-1) of the m-th mineral
S_w	water saturation degree
S_s	specific storage coefficient
T	temperature
T_s	mean temperature of the solid
t	time
V_m	mineral molar volume
w	fluid sink/source per unit volume of medium
x_j	molal concentration of the j-th secondary species
z	elevation
Greek terms	
γ	activity coefficient
δ	constrictivity
ϕ, ϕ_0	porosity and initial porosity, respectively
ϕ^t, ϕ^{t+1}	porosity at times t and $t+1$, respectively
$\boldsymbol{\lambda}$	thermal conductivity tensor
η_m	empirical parameter of kinetics reactions
v_{ji}	stoichiometric coefficient of the i-th primary species in the j-th secondary species
θ	volumetric water content
θ_m	empirical parameter of kinetics reactions
ρ, ρ_s, ρ_m	density of water, solids and bulk porous medium, respectively
τ	medium tortuosity
ψ	pressure head
Ω_m	saturation index (= ion activity product divided by the equilibrium constant)
$\nabla\cdot()$	divergence operator
$\nabla()$	gradient operator

Acknowledgements

This work was funded by the CEBAMA Project of the European Atomic Energy Community's (Euratom) Horizon 2020 Programme (NFRP-2014/2015) under grant agreement # 662147, the

Spanish Ministry of Economy and Competitiveness (Project CGL2016-78281), the FEDER funds, ENRESA (Spain), and the Xunta de Galicia (Galician Regional Government, project ED431C 2017/67). The first author enjoyed a Contract from the FPI Program of the Spanish Ministry of Economy and Competitiveness. We thank the comments and corrections of the three anonymous reviewers who contributed to the improvement of the paper.

References

Allison, J.D., Brown, D.S., Novo-Gradac, K.J., 1991. MINTEQA2/PRODEFA2, a geochemical assessment model for environmental systems: version 3.0 user's manual. United States Environmental Protection Agency, Office of Research and Development, Washington, DC, EPA/600/3-91/021, pp. 106

Alt-Epping, P., Diamond, L.W., Häring, M.O., Ladner, F., Meier, D.B., 2013a. Prediction of water-rock interaction and porosity evolution in a granitoid-hosted enhanced geothermal system, using constraints from the 5 km Basel-1 well. Appl. Geochem., 38, 121-133. https://doi.org/10.1016/j.apgeochem.2013.09.006.

Alt-Epping, P., Waber, H.N., Diamond, L.W., Eichinger, L., 2013b. Reactive transport modeling of the geothermal system at Bad Blumau, Austria: Implications of the combined extraction of heat and CO_2. Geothermics, 45, 18-30. https://doi.org/10.1016/j.geothermics.2012.08.002.

Archie, G., 1942. The electrical resistivity log as an aid in determining some reservoir characteristics. Pet. Trans. AIME 146, 54-62.

Berner, U., Kulik, D.A., Kosakowski, G., 2013. Geochemical impact of a low-pH cement liner on the near field of a repository for spent fuel and high-level radioactive waste. Phys. Chem. Earth, 64, 46-56. https://doi.org/10.1016/j.pce.2013.03.007.

Bildstein, O., Kervévan, C., Lagneau, V., Delaplace, P., Crédoz A., Audigane, P., Perfetti, E., Jacquemet, N., Jullien, M., 2010. Integrative modeling of caprock integrity in the context of CO_2 storage: Evolution of transport and geochemical properties and impact on performance and safety assessment. Oil Gas Sci. Technol., 65(3), 485-502.

Carman, P.C., 1937. Fluid through granular beds. Trans. Inst. Chem. Eng. 15, 150-166.

Chagneau, A., Claret, F., Enzmann, F., Kersten, M., Heck, S., Madé, B., Schäfer, T., 2015. Mineral precipitation-induced porosity reduction and its effect on transport parameters in

512 diffusion-controlled porous media. Geochem. Trans. 16, 13. https://doi.org/10.1186/s12932-
513 015-0027-z.

514 Chen, J.S., Liu, C.W., 2002. Numerical simulation of the evolution of aquifer porosity and species
515 concentrations during reactive transport. Comput. Geosci., 28 (4), 485-499.
516 https://doi.org/10.1016/S0098-3004(01)00084-X.

517 Dai, Z., Wolfsberg, A., Lu, Z., Deng, H., 2009. Scale dependence of sorption coefficients for
518 contaminant transport in saturated fractured rock. Geophys. Res. Lett., 36, L01403.
519 https://doi.org/10.1029/2008GL036516.

520 Dai Z., Wolfsberg, A., Reimus, P., Deng, H., Kwicklis, E., Ding, M., Ware, D., Ye, M., 2012.
521 Identification of sorption processes and parameters for radionuclide transport in fractured rock.
522 J. Hydrol., 414-415, 220-230. https://doi.org/10.1016/j.jhydrol.2011.10.035.

523 Dai, Z., Viswanathan, H., Middleton, R., Pan, F., Ampomah, W., Yang, C., Jia, W., Lee, S.,
524 McPherson, B., Balch, R., Grigg, R., White, M., 2016. CO_2 Accounting and Risk Analysis for
525 CO_2 Sequestration at Enhanced Oil Recovery Sites. Environ. Sci. Technol., 50 (14),
526 7546−7554.

527 Dai, Z., Zhang, Y., Bielicki, J., Amooie, M.A., Zhang, M., Yang, C., Zou, Y., Ampomah, W.,
528 Xiao, T., Jia, W., Middleton, R., Zhang, W., Sun, Y., Moortgat, J., Soltanian, M.R., Stauffer,
529 P., 2018. Heterogeneity-assisted carbon dioxide storage in marine sediments, Appl. Energ.,
530 225, 876-883. https://doi.org/10.1016/j.apenergy.2018.05.038.

531 Deng, H., Molins, S., Trebotich, D., Steefel, C.I., DePaolo, D., 2018. Pore-scale numerical
532 investigation of the impacts of surface roughness: Upscaling of reaction rates in rough
533 fractures. Geochim. Cosmochim. Acta, 239, 374-389.
534 https://doi.org/10.1016/j.gca.2018.08.005.

535 De Windt, L., Pellegrini, D., van der Lee, J., 2004. Coupled modeling of cement/claystone
536 interactions and radionuclide migration. J. Contam. Hydrol., 68(3-4), 165-182.
537 https://doi.org/10.1016/S0169-7722(03)00148-7.

538 De Windt, L., Badreddine, R., Lagneau, V., 2007. Long-term reactive transport modelling of
539 stabilized/solidified waste: from dynamic leaching tests to disposal scenarios. J. Hazard.
540 Mater., 139(3), 529-536. https://doi.org/10.1016/j.jhazmat.2006.03.045.

541 Diamond, L.W., Alt-Epping, P., 2014. Predictive modelling of mineral scaling, corrosion and the
542 performance of solute geothermometers in a granitoid-hosted, enhanced geothermal system.
543 Appl. Geochem., 51, 216-228. https://doi.org/10.1016/j.apgeochem.2014.09.017.

544 Fox, D.T., Guo, L., Fujita, Y., Huang, H., Redden, G., 2015. Experimental and Numerical
545 Analysis of Parallel Reactant Flow and Transverse Mixing with Mineral Precipitation in
546 Homogeneous and Heterogeneous Porous Media. Transp. Porous Med., 111, 605-626.
547 https://doi.org/10.1007/s11242-015-0614-6.

548 Hammond, G.E., Lichtner, P.C., Mills, R.T., 2014. Evaluating the performance of parallel
549 subsurface simulators: An illustrative example with PFLOTRAN. Water Resour. Res., 50(1),
550 208-228. https://doi.org/10.1002/2012WR013483.

551 Hayek, M., Kosakowski, G., Churakov, S., 2011. Exact analytical solutions for a diffusion
552 problem coupled with precipitation–dissolution reaction and feedback of porosity change.
553 Water Resour. Res., 47, W07545. https://doi.org/10.1029/2010WR010321.

554 Hayek, M., Kosakowski, G., Jakob, A., Churakov, S., 2012. A class of analytical solutions for
555 multidimensional species diffusive transport coupled with precipitation–dissolution reactions
556 and porosity changes. Water Resour. Res., 48, W03525.
557 https://doi.org/10.1029/2011WR011663.

558 Hommel, J., Coltman, E., Class, H., 2018. Porosity–Permeability Relations for Evolving Pore
559 Space: A Review with a Focus on (Bio-)geochemically Altered Porous Media. Transp. Porous
560 Med., 124, 589-629. https://doi.org/10.1007/s11242-018-1086-2.

561 Idiart, A., M. Laviña; G. Kosakowski, B. Cochepin; J. C. L. Meeussen, J. Samper, A. Mon, V.
562 Montoya, I. Munier, J. Poonoosamy, L. Montenegro; G. Deissmann, S. Rohmen, L. H
563 Damiani, E. Coene, A Naves, 2020. Benchmark of reactive transport modelling of a low-pH
564 concrete / clay interface. Applied Geochemistry (accepted in press).

565 Jamieson-Hanes, J.H., Amos, R.T., Blowes, D.W., 2012. Reactive transport modeling of
566 Chromium Isotope Fractionation during Cr (IV) Reduction. Environ. Sci. Technol., 46(24),
567 13311-13316. DOI: 10.1021/es3046235.

568 Katz, G.E., Berkowitz, B., Guadagnini, A., Saaltink, M.W., 2011. Experimental and modeling
569 investigation of multicomponent reactive transport in porous media. J. Contam. Hydrol., 120-
570 124, 27-44. https://doi.org/10.1016/j.jconhyd.2009.11.002.

571 Kosakowski, G., Berner, U., 2013. The evolution of clay rock/cement interfaces in a cementitious
572 repository for low and intermediate level radioactive waste. Phys. Chem. Earth, 64, 65-86.
573 https://doi.org/10.1016/j.pce.2013.01.003.

574 Lagneau, V., van der Lee, J., 2010. Operator-splitting-based reactive transport models in strong
575 feedback of porosity change: The contribution of analytical solutions for accuracy validation
576 and estimator improvement. J. Contam. Hydrol., 112(1-4), 118-129.

577 Lalan, P., Dauzères, A., DeWindt, L., Bartier, D., Sammaljärvi, J., Barnichon, J.D., Techer, I.,
578 Detilleux, V., 2016. Impact of a 70 °C temperature on an ordinary Portland cement
579 paste/claystone interface: an in situ experiment. Cement Concr. Res. 83, 164–178.

580 Lichtner, P.C., 1996. Continuum formulation of multicomponent multiphase reactive transport.
581 In: Lichtner, P.C., Steefel, C.I., Oelkers, E.H. (Eds.), Mineralogical Society of America,
582 Washington, 34 (Chapter 1), pp. 1-81.

583 Lichtner, P., Hammond, G.E., Lu, C., Karra, S., Bisht, G., Andre, B., Mills, R., Kumar, J.,
584 Frederick, J.M., 2018. PFLOTRAN Documentation. Release 1.1. 594 pp.

585 Lu, C., Samper, J., Fritz, B., Clement, A., Montenegro, L., 2011. Interactions of corrosion
586 products and bentonite: An extended multicomponent reactive transport model. Phys. Chem.
587 Earth Pt. A/B/C, 36 (17-18), 1661–1668. https://doi.org/10.1016/j.pce.2011.07.013.

588 Marty, N.C.M., Tournassat, C., Burnol, A., Giffaut, E., Gaucher, E.C., 2009. Influence of reaction
589 kinetics and mesh refinement on the numerical modelling of concrete/clay interactions. J.
590 Hydrol., 364, 58-72. https://doi.org/10.1016/j.jhydrol.2008.10.013.

591 Mayer, K.U., Frind, E.O., Blowes D.W., 2002. Multicomponent reactive transport modeling in
592 variably saturated porous media using a generalized formulation for kinetically controlled
593 reactions. Water Resour. Res., 38(9), 1174. https://doi.org/10.1029/2001WR000862.

594 Millington, R.J., Quirk, J.P., 1961. Permeability of porous solids. Trans. Faraday Soc., 57, 1200-
595 1207.

596 Min, T., Gao, Y., Chen, L., Kang, Q., Tao, W.W., 2016. Changes in porosity, permeability and
597 surface area during rock dissolution: Effects of mineralogical heterogeneity. Inter. J. Heat
598 Mass Transfer, 103, 900-913. https://doi.org/10.1016/j.ijheatmasstransfer.2016.07.043.

599 Molinero, J., Samper, J., Zhang, G., Yang, C., 2004. Biogeochemical reactive transport model of
600 the redox zone experiment of the Äspö hard rock laboratory in Sweden. Nucl. Technol.,
601 148(2), 151-165. https://doi.org/10.13182/NT04-A3555.

602 Molins, S., 2015. Reactive interfaces in direct numerical simulation of pore-scale processes. Rev.
603 Mineral. Geochem., 80, 461-481. https://doi.org/10.2138/rmg.2015.80.14.

604 Mon, A., Samper, J., Montenegro, L., Naves, A., Fernández, J., 2017. Long-term non-isothermal
605 reactive transport model of compacted bentonite, concrete and corrosion products in a HLW
606 repository in clay. J. Contam. Hydrol., 197, 1-16.
607 https://doi.org/10.1016/j.jconhyd.2016.12.006.

608 Todaka, N., Xu, T., 2017. Reactive transport simulation to assess geochemical impact of
609 impurities on CO2 injection into siliciclastic reservoir at the Otway site, Australia. Int. J.
610 Greenh. Gas Con., 66, 177–189. https://doi.org/10.1016/j.ijggc.2017.07.014.

611 Parkhurst, D.L., Kipp, K.L., Engesgaard, P., Charlton S.R., 2002. PHAST - A program for
612 simulating ground-water flow and multicomponent geochemical reactions. U.S. Geological
613 Survey, Denver, Colorado.

614 Poonoosamy, J., Kosakowski, G., Van Loon, L.R., Mäder, U., 2015. Dissolution-precipitation
615 processes in tank experiments for testing numerical models for reactive transport calculations:
616 Experiments and modelling. J. Contam. Hydrol., 177, 1-17.
617 https://doi.org/10.1016/j.jconhyd.2015.02.007.

618 Poonoosamy, J., Curti, E., Kosakowski, G., Grolimund, D., Van Loon, L.R., Mäder, U., 2016.
619 Barite precipitation following celestite dissolution in a porous medium: A SEM/BSE and μ-
620 XRD/XRF study. Geochim. Cosmochim. Acta 182, 131-144.
621 https://doi.org/10.1016/j.gca.2016.03.011.

622 Poonoosamy, J., Wanner, C., Alt Epping, P., Águila, J.F., Samper, J., Montenegro, L., Xie, M.,
623 Su, D., Mayer, K.U., Mäder, U., Van Loon, L.R., Kosakowski, G., 2018. Benchmarking of
624 reactive transport codes for 2D simulations with mineral dissolution–precipitation reactions
625 and feedback on transport parameters. Computat. Geosci. https://doi.org/10.1007/s10596-018-
626 9793-x.

627 Samper, J., Dai, Z., Molinero, J., García-Gutiérrez, M., Missana, T., Mingarro, M., 2006. Inverse
628 modeling of tracer experiments in FEBEX compacted Ca-bentonite. Phys. Chem. Earth Pt.
629 A/B/C, 31 (10-14), 640-648. https://doi.org/10.1016/j.pce.2006.04.013.

630 Samper J., Yang, C., 2006. Stochastic analysis of transport and multicomponent competitive
631 monovalent cation exchange in aquifers. Geosphere, 2(2), 102-112.
632 https://doi.org/10.1130/GES00030.1.

633 Samper, J., Lu, C., Montenegro, L., 2008. Reactive transport model of interactions of corrosion
634 products and bentonite. Phys. Chem. Earth Pt. A/B/C, 33(1), S306-S316.
635 https://doi.org/10.1016/j.pce.2008.10.009.

636 Samper, J., Xu, T., Yang, C., 2009. A sequential partly iterative approach for multicomponent
637 reactive transport with CORE^{2D}. Computat. Geosci., 13:301 https://doi.org/10.1007/s10596-
638 008-9119-5.

639 Samper, J., Yang, C., Zheng, L., Montenegro, L., Xu, T., Dai, Z., Zhang, G., Lu, C., Moreira, S.,
640 2011. CORE^{2D}V4: A code for water flow, heat and solute transport, geochemical reactions,
641 and microbial processes. In: Zhang, F., Yeh, G.-T., Parker, C., Shi, X. (Eds.), Chapter 7 of the
642 Electronic Book Groundwater Reactive Transport Models. Bentham Science Publishers.
643 ISBN: 978-1-60805-029 1, pp 161-186.

644 Samper, J., Naves, A., Montenegro, L., Mon, A., 2016. Reactive transport modelling of the long-
645 term interactions of corrosion products and compacted bentonite in a HLW repository in
646 granite: Uncertainties and relevance for performance assessment. Appl. Geochem., 67, 42-51.
647 https://doi.org/10.1016/j.apgeochem.2016.02.001.

648 Samper, J, A Mon, L Montenegro, 2018.

649 A revisited thermal, hydrodynamic, chemical and mechanical model of compacted bentonite for
650 the entire duration of the FEBEX in situ test, Applied Clay Sciences, Vol 160: 58-70.
651 doi.org/10.1016/j.clay.2018.02.019.

652 Seigneur, N., L'Hôpital, E., Dauzères, A., Sammaljärvi, J., Voutilainen, J., Labeau, P.E., Dubus,
653 A., Detilleux, V., 2017. Transport properties evolution of cement model system under
654 degradation - Incorporation of a pore-scale approach into reactive transport modelling. Phys.
655 Chem. Earth Pt. A/B/C, 99, 95-109. https://doi.org/10.1016/j.pce.2017.05.007.

656 Seigneur, N., Lagneau, V., Corvisier, J., Dauzères, A., 2018. Recoupling flow and chemistry in
657 variably saturated reactive transport modelling - An algorithm to accurately couple the
658 feedback of chemistry on water consumption, variable porosity and flow. Adv. Water. Resour.,
659 122, 355-366. https://doi.org/10.1016/j.advwatres.2018.10.025.

660 Seigneur, N., Mayer, U., Steefel, C., 2019. Reactive Transport in Evolving Porous Media, Rev.
661 Mineral. Geochem., 85 (1), 197-238. https://doi.org/10.2138/rmg.2019.85.7.

662 Shafizadeh, A., Gimmia, T., Van Loon, L.R., Kaestner, A.P., Mäder, U.K., Churakov, S.V., 2020.
663 Time-resolved porosity changes at cement-clay interfaces derived from neutron imaging.
664 Cement Concrete Res., 127. https://doi.org/10.1016/j.cemconres.2019.105924.

665 Shao, H., Kosakowski, G., Berner, U., Kulik, D.A., Mäder, U., Kolditza, O., 2013. Reactive
666 transport modeling of the clogging process at Maqarin natural analogue site. Phys. Chem.
667 Earth Pt. A/B/C, 64, 21-31. https://doi.org/10.1016/j.pce.2013.01.002.

668 Simunek, J., van Genuchten, M.T., Sejna, M., 2008. Development and applications of the
669 HYDRUS and STANMOD software packages and related codes. Vadose Zone J., 7(2), 587-
670 600.

671 Simunek, J., Jacques, Twarakavi, N.K.C., van Genuchten M.T., 2009. Selected HYDRUS
672 modules for modeling subsurface flow and contaminant transport as influenced by biological
673 processes at various scales. Biologia, 64(3), 465-469. https://doi.org/10.2478/s11756-009-
674 0106-7.

675 Soler, J.M., Samper, J., Yllera, A., Hernández, A., Quejido, A., Fernández, M., Yang, C., Naves,
676 A., Hernán, P., Wersin, P., 2008. The DI-B in-situ diffusion experiment at Mont Terri: results
677 and modelling. Phys. Chem. Earth, 33(1), S196-S207.
678 https://doi.org/10.1016/j.pce.2008.10.010.

679 Steefel, C.I., 2001. CRUNCH: Software for modeling multicomponent, multidimensional
680 reactive transport, user's guide. Rep. UCRL-MA-143182, Lawrence Livermore Nat. Lab.,
681 Livermore, California.

682 Steefel, C.I., De Paolo, D.J., Lichtner, P.C., 2005. Reactive transport modeling: an essential tool
683 and a new research approach for earth sciences. Earth Planet. Sc. Lett., 240 (3-4), 539-558.
684 http://dx.doi.org/10.1016/j.epsl.2005.09.017.

685 Steefel, C.I., Appelo, C.A.J., Arora, B., Jacques, D., Kalbacher, T., Kolditz, O., Lagneau, V.,
686 Lichtner, P.C., Mayer K.U., Meeussen J.C.L., Molins, S., Moulton, D., Shao, H., Simunek, J.,
687 Spycher, N., Yabusaki, S.B., Yeh, G.T., 2015. Reactive transport codes for subsurface
688 environmental simulation. Comput. Geosci., 19, 445–478. https://doi.org/10.1007/s10596-
689 014-9443-x.

690 van der Lee, J., De Windt L., Lagneau V., Goblet P., 2003. Module-oriented modeling of reactive
691 transport with HYTEC. Comput. Geosci., 29(3), 265-275. https://doi.org/10.1016/S0098-
692 3004(03)00004-9.

693 Wanner, C., Eggenberger, U., Mäder, U., 2012. A chromate-contaminated site in southern
694 Switzerland-part 2: Reactive transport modeling to optimize remediation options. Appl.
695 Geochem., 27(3), 655-662. https://doi.org/10.1016/j.apgeochem.2011.11.008.

696 Wanner, C., Sonnenthal, E.L., 2013. Assessing the control on the effective kinetic Cr isotope
697 fractionation factor: A reactive transport modeling approach. Chem. Geol., 337-338, 88 98.
698 https://doi.org/10.1016/j.chemgeo.2012.11.008.

699 Wanner, C., Peiffer, L., Sonnenthal, E.L., Spycher, N., Iovenitti, J., Kennedy, B.M., 2014.
700 Reactive transport modeling of the Dixie Valley geothermal area: Insights on flow and
701 geothermometry. Geothermics, 51, 130-141.
702 https://doi.org/10.1016/j.geothermics.2013.12.003.

703 Wanner, C., Eichinger, F., Jahrfeld, T., Diamond, L.W., 2017. Unraveling the Formation of Large
704 Amounts of Calcite Scaling in Geothermal Wells in the Bavarian Molasse Basin: A Reactive
705 Transport Modeling Approach. Proced. Earth Plan. Sc., 17, 344-347.
706 https://doi.org/10.1016/j.proeps.2016.12.087.

707 Wei, X., Li, W., Tian, H., Xu, H., Xu, T., 2015. THC-MP: High performance numerical
708 simulation of reactive transport and multiphase flow in porous media. Comput. Geosci., 80,
709 26-37. https://doi.org/10.1016/j.cageo.2015.03.014.

710 Wolery, T.J., 1992. EQ3/6, a software package for geochemical modeling of aqueous systems:
711 package overview and installation guide (version 7.0). Technical Report UCRL-MA-110662-
712 Pt 1. Lawrence Livermore National Laboratory, CA, USA.

713 Wolfsberg, A., Dai, Z., Reimus, P., Xiao, P., Ware, D., 2017. Colloid-Facilitated Plutonium
714 Transport in Fractured Tuffaceous Rock. Environ. Sci. Technol. 51 (10), 5582-5590.
715 https://doi.org/10.1021/acs.est.7b00968.

716 Xie, M., Mayer, K.U., Claret, F., Alt-Epping, P., Jacques, D., Steefel, C., Chiaberge, C., Simunek,
717 J., 2015. Implementation and evaluation of permeability-porosity and tortuosity-porosity
718 relationships linked to mineral dissolution-precipitation. Computat. Geosci., 19(3), 655-671.
719 https://doi.org/10.1007/s10596-014-9458-3.

720 Xu, T., Samper, J., Ayora, C., Manzano, M., Custodio, E., 1999. Modeling of Non-Isothermal
721 Multi-Component Reactive Transport in Field Scale Porous Media Flow System. J. Hydrol.,
722 214(1-4), 144-164. https://doi.org/10.1016/S0022-1694(98)00283-2.

723 Xu, T., Sonnenthal E., Spycher N., Pruess K., 2004. TOUGHREACT user's guide: A simulation
724 program for non-isothermal multiphase reactive geochemical transport in variable saturated
725 geologic media. Lawrence Berkeley Natl. Lab., Berkeley, Calif. 192 pp.

726 Xu, T., Sonnenthal E., Spycher N., Pruess K., 2006. TOUGHREACT - A simulation program for
727 non-isothermal multiphase reactive geochemical transport in variably saturated geologic
728 media: Applications to geothermal injectivity and CO_2 geological sequestration. Comput.
729 Geosci., 32(2), 145-165. https://doi.org/10.1016/j.cageo.2005.06.014.

730 Xu, T., Spycher N., Sonnenthal E., Zhang G., Zheng L., Pruess K., 2011. TOUGHREACT version
731 2.0: A simulator for subsurface reactive transport under non-isothermal multiphase flow
732 conditions. Comput. Geosci., 37(6), 763-774. https://doi.org/10.1016/j.cageo.2010.10.007.

733 Xu, T., Hou, Z., Jia, X., Spycher, N., Jiang, Z., Feng, B., Na, J., Yuan, Y., 2016, Classical and
734 integrated multicomponent geothermometry at the Tengchong geothermal field, Southwestern
735 China. Environ. Earth Sc., 75:1502. https://doi.org/10.1007/s12665-016-6298-6.

736 Yang, C., Samper, J., Molinero, M., 2008. Inverse Microbial and Geochemical Reactive Transport
737 Models in Porous Media. Phys. Chem. Earth Pt. A/B/C, 33(14-16), 1026-1034.
738 https://doi.org/10.1016/j.pce.2008.05.016.

739 Yang, Y-M., Small, M.J., Junker, B., Bromhal, G.S., Strazisar, B., Wells, A., 2011. Bayesian
740 hierarchical models for soil CO_2 flux and leak detection at geologic sequestration sites.
741 Environ. Earth Sci., 64(3), 787–798. https://doi.org/10.1007/s12665-011-0903-5.

742 Yang, C., Dai, Z., Romanak, K.D., Hovorka, S.D., Treviño, R.H., 2014. Inverse modeling of
743 water-rock-CO_2 batch experiments: Potential impacts on groundwater resources at carbon
744 sequestration sites. Environ Sci. Technol., 48(5), 2798–2806

745 Yeh, G.T., Gwo, J.P., Siegel, M.D., Li, M.H., Fang, Y., Zhang, F., Luo, W., Yabusaki, S.B., 2013.
746 Innovative mathematical modeling in environmental remediation. J. Environ. Radioactiv.,
747 119, 26-38. https://doi.org/10.1016/j.jenvrad.2011.06.010.

748 Yllera, A., Hernández, A., Mingarro, M., Quejido, A., Sedano, L.A., Soler, J.M., Samper, J.,
749 Molinero, J., Barcala, J.M., Martín, P.L., Fernández M., Wersin P., Rivas P., Hernán P., 2004.
750 DI-B experiment: planning, design and performance of an in situ diffusion experiment in the
751 Opalinus Clay formation. Appl. Clay Sci., 26(1-4), 181-196.
752 https://doi.org/10.1016/j.clay.2003.12.007.

753 Zhang, G., Samper, J., Montenegro, L., 2008. Coupled thermo-hydro-bio-geochemical reactive
754 transport model of the CERBERUS heating and radiation experiment in Boom clay. Appl.
755 Geochem., 23(4), 932-949. https://doi.org/10.1016/j.apgeochem.2007.09.010.

756 Zheng, L., Samper, J., Montenegro, L., Fernández, A.M., 2010. A coupled THMC model of a
757 heating and hydration laboratory experiment in unsaturated compacted FEBEX bentonite. J.
758 Hydrol., 386(1-4), 80-94. https://doi.org/10.1016/j.jhydrol.2010.03.009.

759 Zheng, L., Samper, J., Montenegro, L., 2011. A coupled THC model of the FEBEX in situ test
760 with bentonite swelling and chemical and thermal osmosis. J. Contam. Hydrol., 126(1-2), 45-
761 60. https://doi.org/10.1016/j.jconhyd.2011.06.003.

762 Zheng, L., Rutqvist, J., Xu, H., Birkholzer J.T., 2017. Coupled THMC models for bentonite in an
763 argillite repository for nuclear waste: Illitization and its effect on swelling stress under high
764 temperature. Eng. Geol., 230, 118-129. https://doi.org/10.1016/j.enggeo.2017.10.002.

765

766

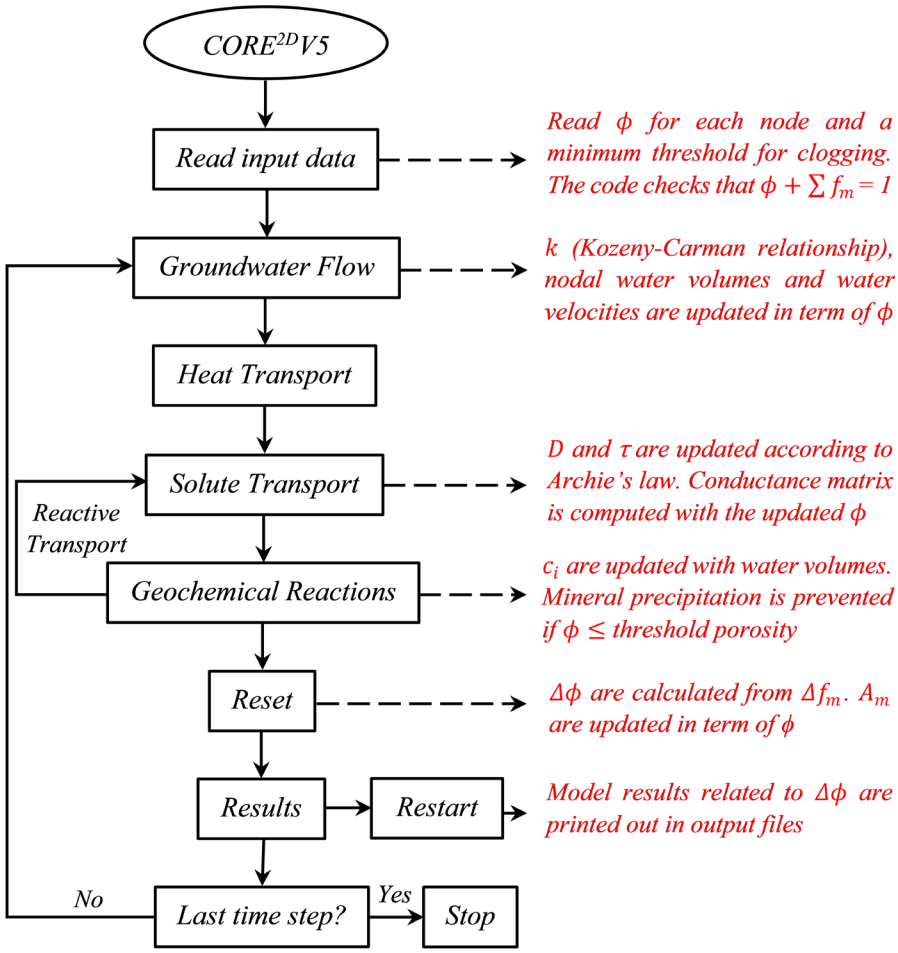

767

768 **Fig. 1.** Main flowchart of CORE^{2D}V5. Red text shows the main modifications performed in the
769 extended code to take into account the changes in the porosity and update flow, transport and
770 chemical parameters. The definition of all the symbols can be found in the Nomenclature.

771

772

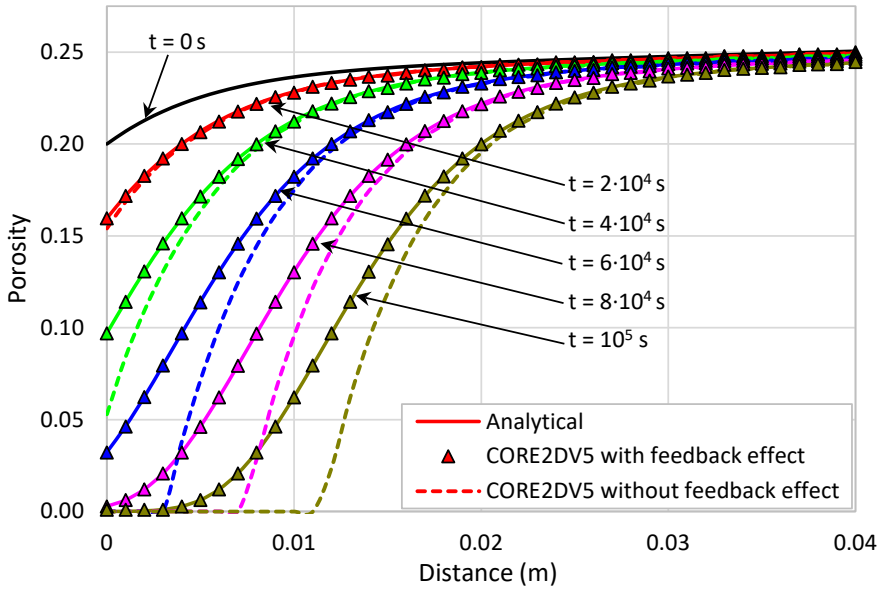

773

774 **Fig. 2.** Comparison of the computed porosity profiles with (symbols) and without the PFE
775 (discontinuous lines) and analytical solutions (continuous lines) at selected times for the 1-D
776 verification test case.

777

778

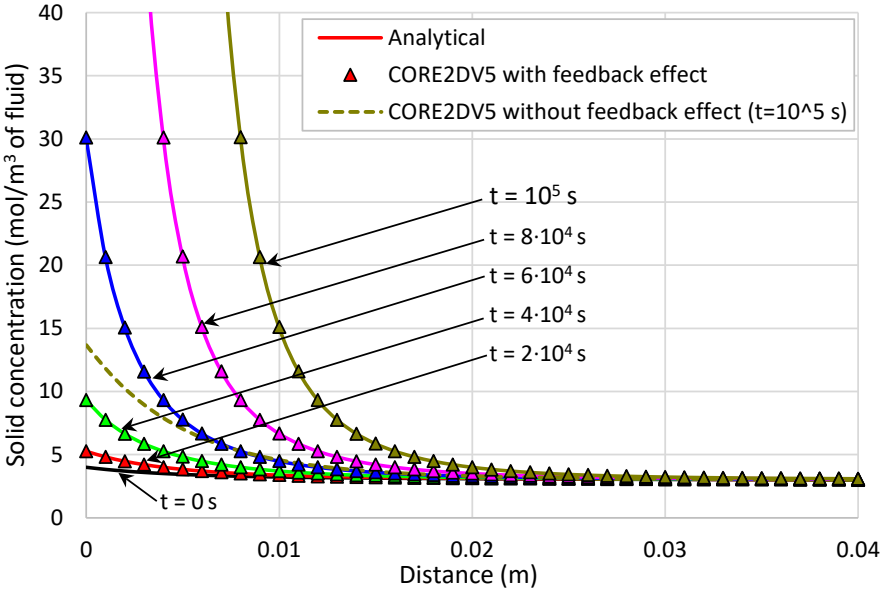

779

780 **Fig. 3.** Comparison of the computed mineral concentration profiles with feedback the PFE
781 (symbols) and analytical solutions (continuous lines) at selected times for the 1-D verification
782 test case. The discontinous line shows the computed mineral concentration profiles at the end of
783 the simulation at $t = 10^5$ s without the PFE.

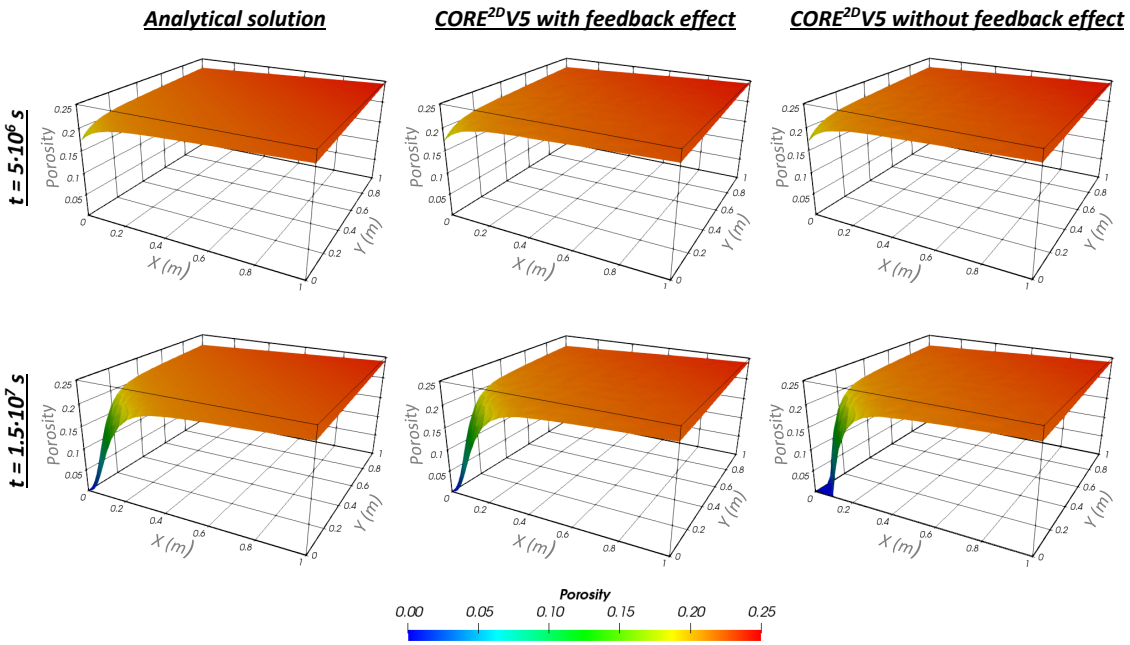

784

785 **Fig. 4.** 3-D plots of the spatial distribution of the porosity calculated with analytical solutions
786 (left) and with CORE^{2D}V5 with (intermediate) and without (right) the without the PFE after
787 $5 \cdot 10^6$ s (top) and $1.5 \cdot 10^7$ s (bottom) for the 2-D verification test case.

788

789

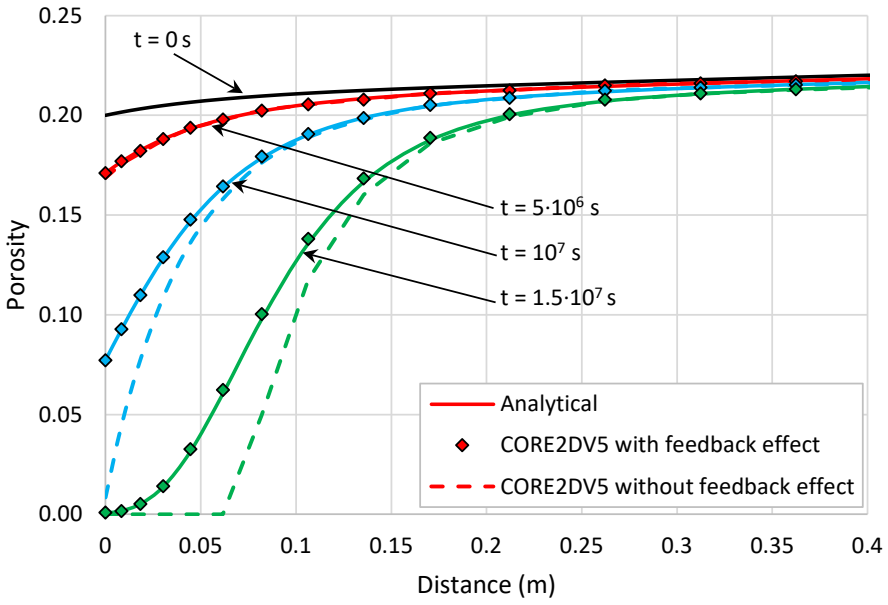

790

Fig. 5. Comparison of the computed porosity profiles with (symbols) and without the without the PFE (discontinuous lines) and analytical solutions (continuous lines) at selected times for the 2-D verification test case.

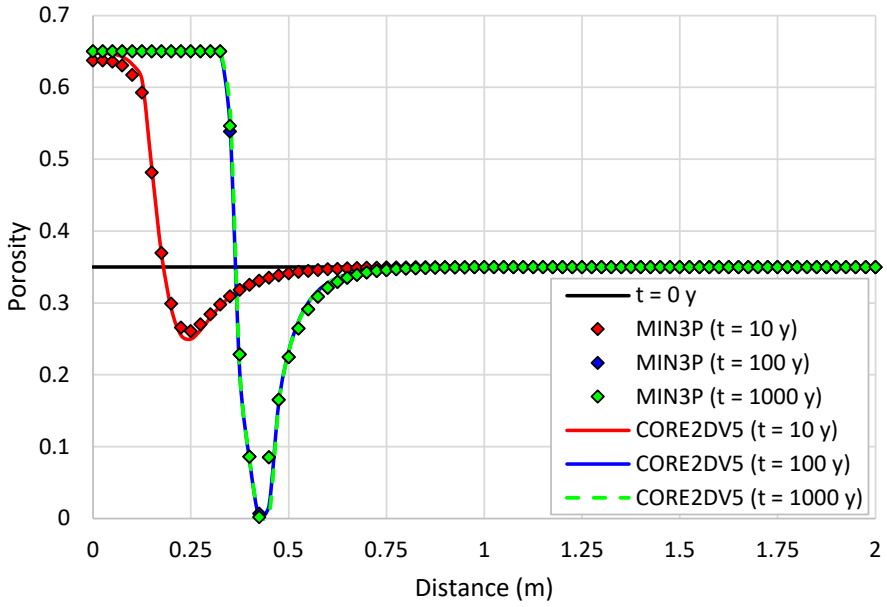

Fig. 6. Comparison of the porosity profiles computed with MIN3P and CORE^{2D}V5 at 10, 100 and 1000 years for the benchmark test case.

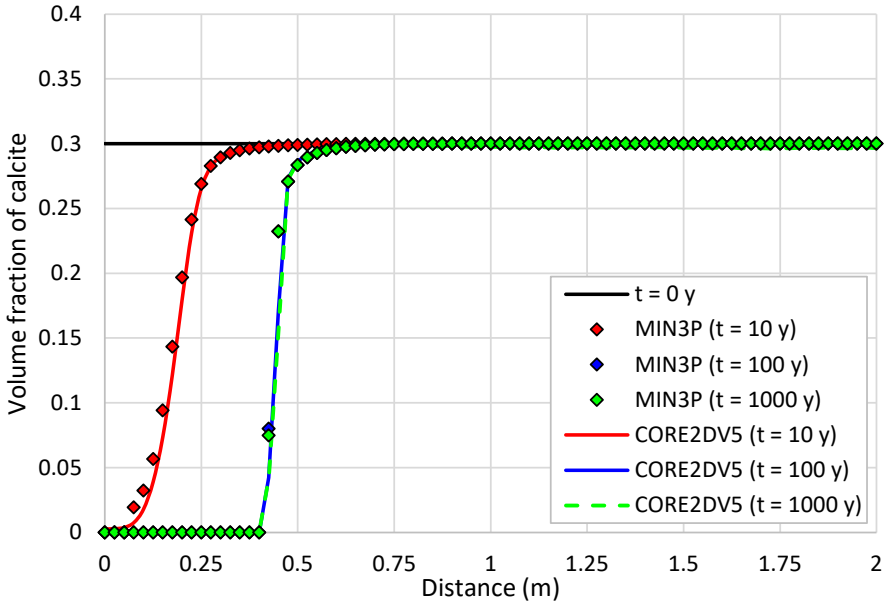

Fig. 7. Comparison of the calcite volume fraction profiles computed with MIN3P and CORE^{2D}V5 at 10, 100 and 1000 years for the benchmark test case.

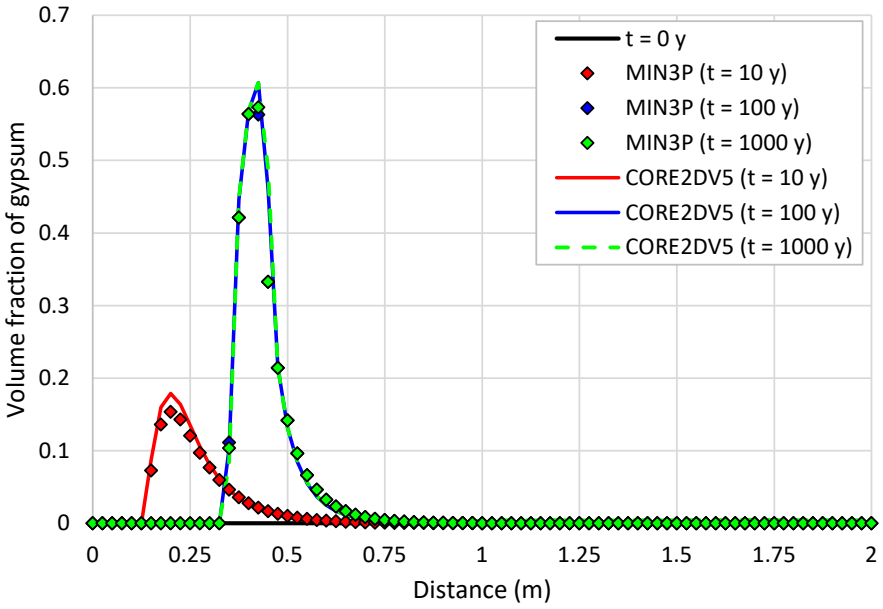

Fig. 8. Comparison of the gypsum volume fraction profiles computed with MIN3P and CORE^{2D}V5 at 10, 100 and 1000 years for the benchmark test case.

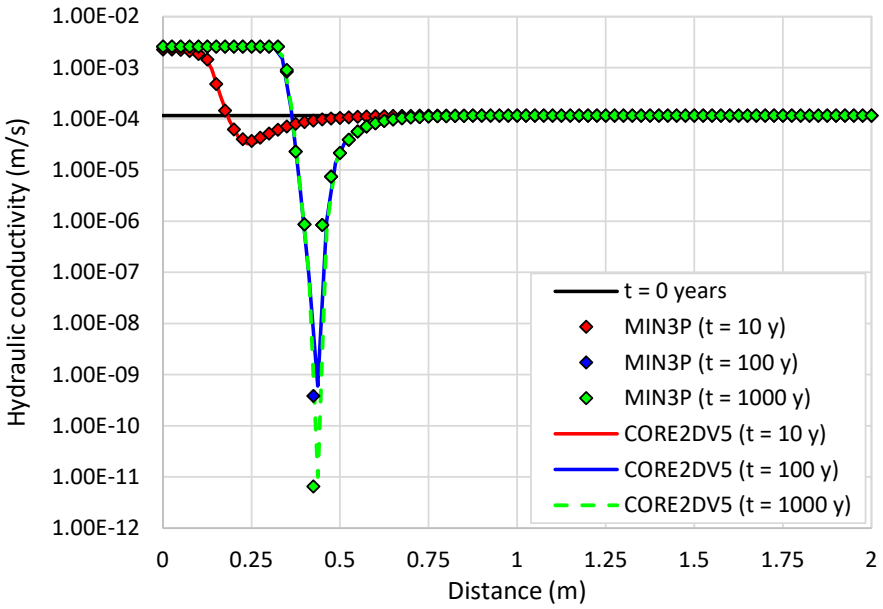

Fig. 9. Comparison of the hydraulic conductivity profiles computed with MIN3P and CORE^{2D}V5 at 10, 100 and 1000 years for the benchmark test case.

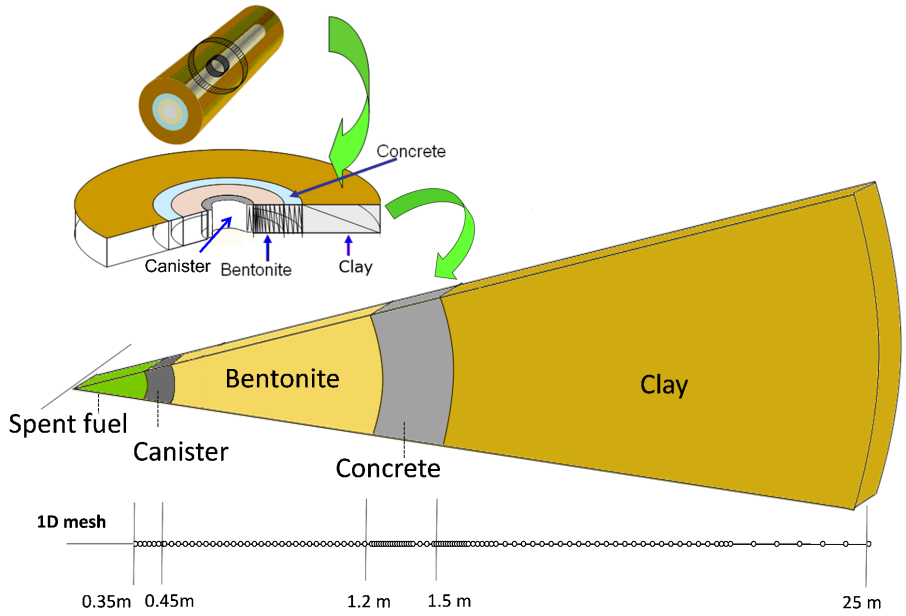

Fig. 10. Scheme of the multibarrier system of a radioactive waste repository in clay according to the Spanish Reference Concept and 1-D finite element grid which accounts for the canister, the bentonite barrier, the concrete liner and the clay formation (Mon et al., 2017).

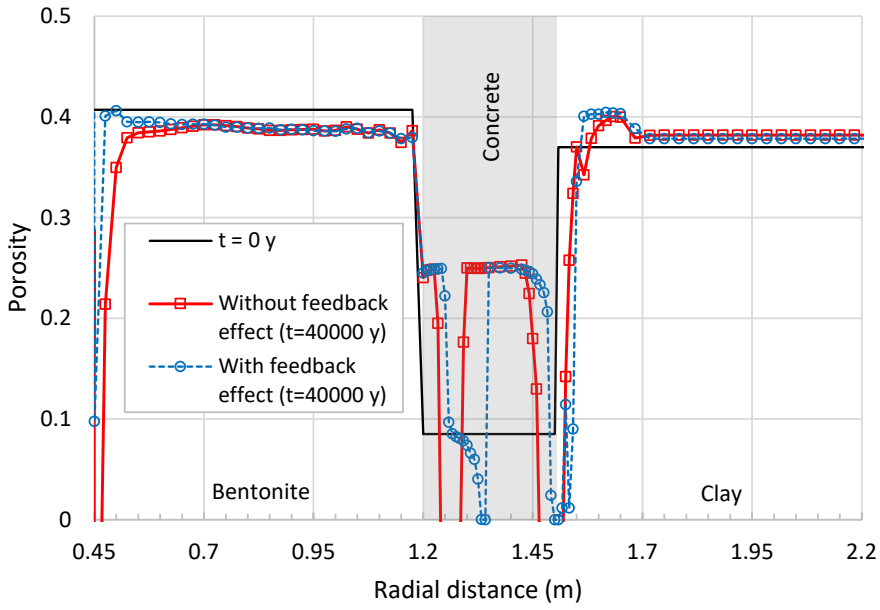

Fig. 11. Radial distribution of the porosity at $t = 0$ and $4 \cdot 10^4$ years with and without the without the PFE.

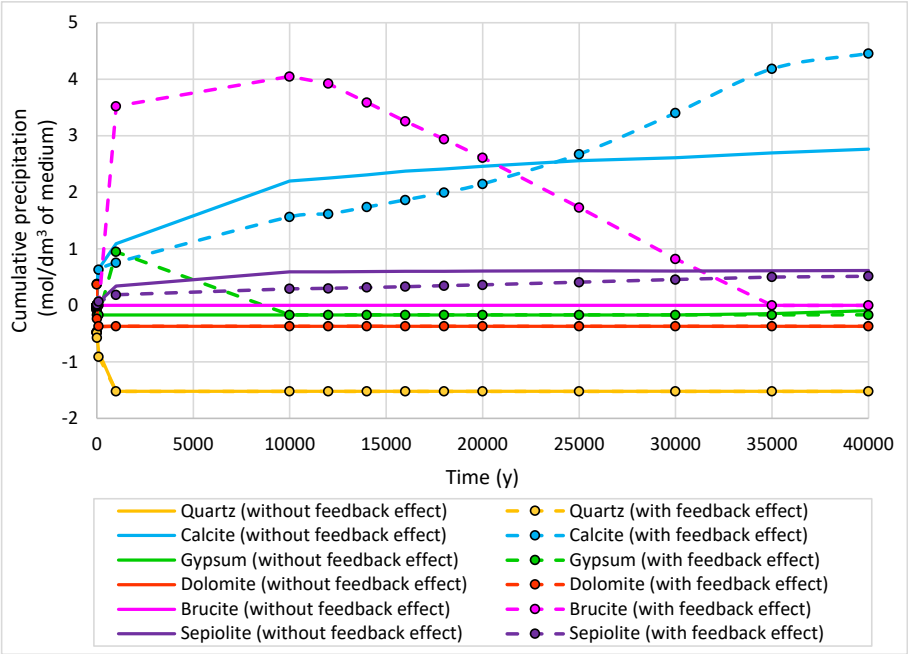

824

825 **Fig. 12.** Time evolution of the cumulative mineral dissolution/precipitation in the clay
826 formation near the concrete interface (r = 1.525 m) computed with and without the without the
827 PFE (positive for precipitation and negative for dissolution).

828

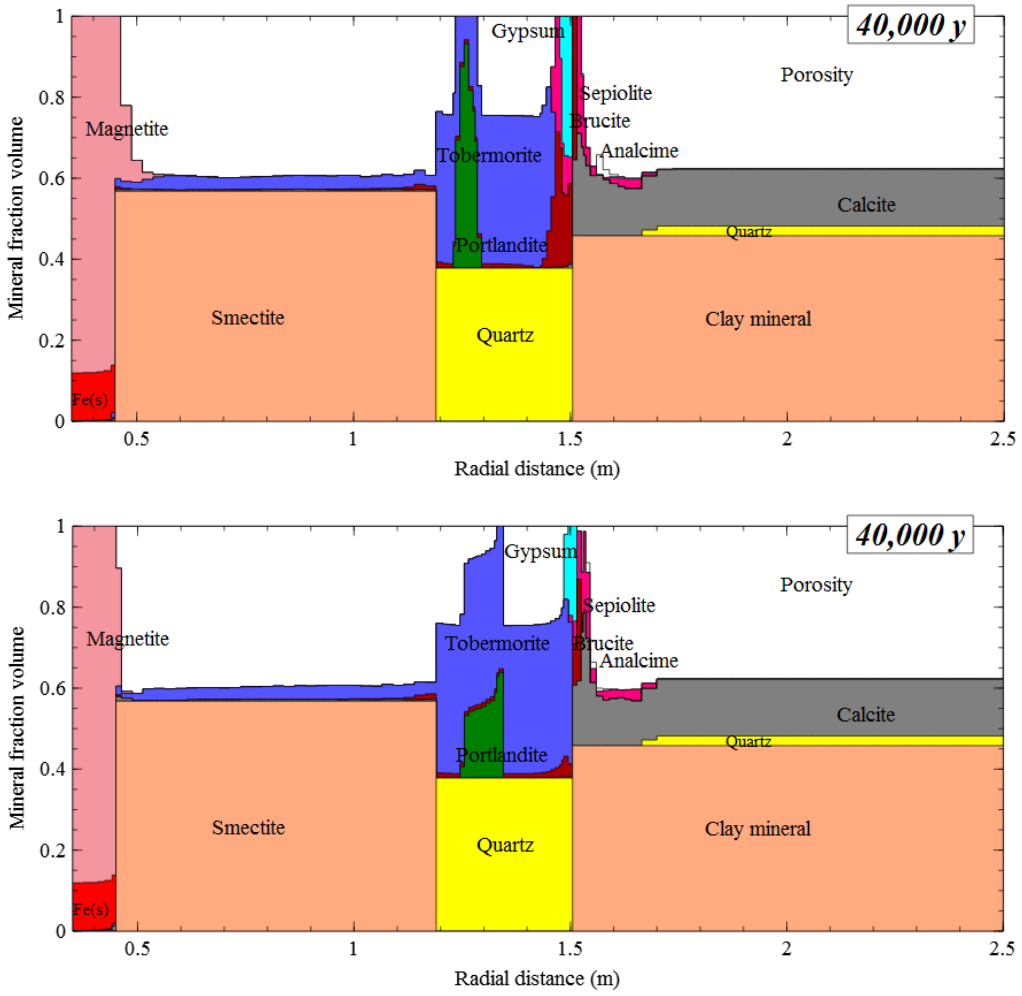

829

830 **Fig. 13.** Mineral volume fractions at $t = 4 \cdot 10^4$ years computed without (top) and with (bottom)
831 the PFE.

832

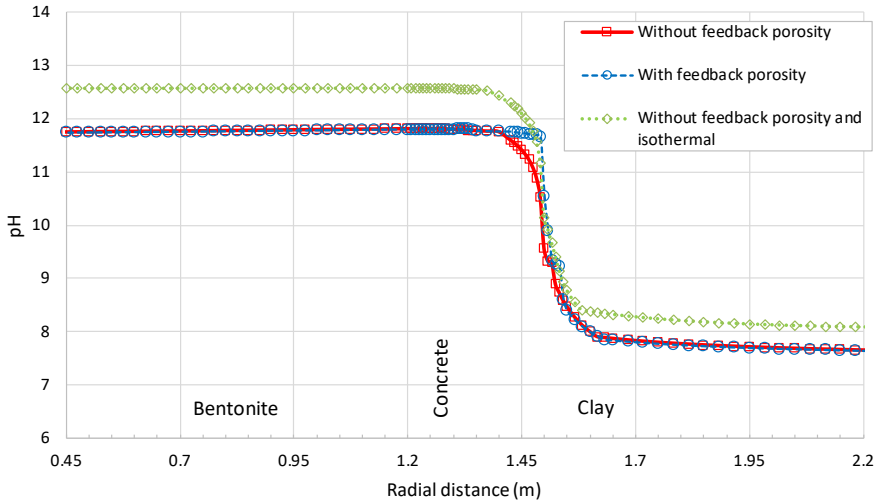

Fig. 14. Radial distribution of the pH computed at $t = 10^4$ years with and without the PFE under non-isothermal conditions and without the PFE under isothermal conditions.

Table 1. Parameters used in 1-D and 2-D numerical models performed to verify the code CORE^{2D}V5 with the analytical solutions (Hayek et al., 2011, 2012).

Parameter	1-D model	2-D model
D_0 (m^2/s)	10^{-9}	10^{-9}
log(K)	-0.16	-0.41
r_m (mol/m^2/s)	10^{-10}	10^{-12}
V_m (m^3/mol)	1	1
A_0 (m^2/m^3)	$5 \cdot 10^3$	10^3

Table 2. Physical and kinetic mineral parameters in the benchmark test case.

Mineral	r_m^0 (m^2 mineral/L bulk)	Density (g/cm^3)	Mol weight (g/mol)	Molar volume (cm^3/mol)	Update type
Calcite	$5 \cdot 10^{-8}$	2.71	100.09	36.93	Two third
Gypsum	$5 \cdot 10^{-8}$	2.32	172.17	74.21	Constant

Table 3. Chemical composition of the initial and boundary waters used in CORE^{2D}V5 in the benchmark test case.

Primary components	Unit	Initial condition	Boundary condition
pH	[-]	9.33	3.0
Ca^{2+}	[mol / L]	$1.70 \cdot 10^{-4}$	$1.00 \cdot 10^{-4}$
CO_3^{2-}	[mol / L]	$2.70 \cdot 10^{-4}$	$1.00 \cdot 10^{-2}$
SO_4^{2-}	[mol / L]	$1.70 \cdot 10^{-4}$	$2.00 \cdot 10^{-1}$
Na^{+}	[mol / L]	$3.20 \cdot 10^{-4}$	$3.96 \cdot 10^{-1}$

Table 4. Reactions and equilibrium constants for aqueous complexation and mineral dissolution/precipitation reactions at 25ºC used in CORE^{2D}V5 in the benchmark test case (Allison et al., 1991; Xie et al., 2015).

	Aqueous complexes	Log K (25ºC)
	$CaCO_3(aq) + H^+ \Leftrightarrow Ca^{2+} + HCO_3^-$	7.1100
	$CaHCO_3^+ \Leftrightarrow Ca^{2+} + HCO_3^-$	-1.1100
	$CaOH^+ + H^+ \Leftrightarrow Ca^{2+} + H_2O$	12.7800
	$CaSO_4(aq) \Leftrightarrow Ca^{2+} + SO_4^{2-}$	-2.3090
	$CaHSO_4^+ \Leftrightarrow Ca^{2+} + SO_4^{2-} + H^+$	-3.0680
	$CO_3^{2-} + H^+ \Leftrightarrow HCO_3^-$	10.3300
	$CO_2(aq) + H_2O \Leftrightarrow H^+ + HCO_3^-$	-6.3510
	$OH^- + H^+ \Leftrightarrow H_2O$	13.9980
	$NaSO_4^- \Leftrightarrow Na^+ + SO_4^{2-}$	-0.7000
	$NaCO_3^- \Leftrightarrow Na^+ + CO_3^{2-}$	-1.2680
	$NaHCO_3(aq) \Leftrightarrow Na^+ + HCO_3^-$	-0.2500
	$H_2SO_4(aq) \Leftrightarrow SO_4^{2-} + 2H^+$	1.0209
	$HSO_4^- \Leftrightarrow H^+ + SO_4^{2-}$	-1.9870
	Minerals	**Log K (25ºC)**
Calcite	$CaCO_3(s) + H^+ \Leftrightarrow Ca^{2+} + HCO_3^-$	1.8550
Gypsum	$CaSO_4 \cdot 2H_2O(s) \Leftrightarrow Ca^{2+} + SO_4^{2-} + 2H_2O$	-4.5800

Table 5. Thermal and hydrodynamic parameters of the canister, the bentonite barrier, the concrete liner and the clay formation.

Parameter	Carbon steel canister	Bentonite barrier	Concrete liner	Clay formation
Hydraulic conductivity (m/s)	$2.75 \cdot 10^{-14}$	$2.75 \cdot 10^{-14}$	$3.39 \cdot 10^{-12}$	$4.19 \cdot 10^{-12}$
Initial porosity	0.407	0.407	0.085	0.37
Effective diffusion (m^2/s)	$4.08 \cdot 10^{-11}$	$4.08 \cdot 10^{-11}$	$8.56 \cdot 10^{-12}$	$5.01 \cdot 10^{-11}$
Density of the solids (kg/m^3)	7860	2700	2513	2778
Specific heat capacity (J/kg^oK)	477.66	846.4	1374.32	1118.7

859

860

861